# Upscaling Acoustic Wave Equation using Renormalization Group Theory

Ajay Malkoti* †, Shravan M. Hanasoge*, and René-Édouard Plessix‡

## ABSTRACT

Seismic waves interact with a broad range of heterogeneities as they propagate through the Earth. Simulating this full range of scales for wave propagation requires capturing heterogeneities of all scales, which can be computationally unaffordable. In such cases, we rely on macroscopic representations of media obtained through an upscaling process that preserves the effects of small-scale heterogeneities (in comparison to the wavelengths of interest). Here we discuss the application of the renormalization-group (RG) theory-based upscaling to the two-dimensional acoustic wave equation. RG-based upscaling requires constructing a special Fourier operator and is implemented using a domain-decomposition in conjunction with an "expansion and truncation" method to mitigate edge effects. We test this upscaling method on several benchmark models and in the context of reverse-time migration. The upscaled models obtained using this method show a good consistency for generated waveforms, while the runtime for simulations is reduced by at least an order of magnitude.

## INTRODUCTION

Seismic imaging techniques such as reverse-time migration, least-squares reverse-time migration or full waveform inversion require the simulation of wave propagation inside an idealized Earth. Wave propagation is sensitive to Earth's parameter variations inside a Fresnel volume (Spetzler and Snieder, 2004), due to the finite-frequency nature of the seismic experiment. Numerically, we cannot account for all scales of the heterogeneities since it would be computationally very expensive. We, therefore, work with a macroscopic representation of the Earth's parameters. When we discretize the wave equation using a numerical scheme, e.g., a finite-difference method, the representation of the solution and model parameters are generally dictated by the cell size or grid spacing, since we associate material parameter(s), e.g., velocities, density, etc., to each cell. Grid spacing is typically defined in terms of a fraction of the (minimum) wavelength in order to limit the numerical dispersion of the scheme (Dablain, 1986). As a rule of thumb, second, fourth, and eighth-order schemes require around 16, 8, and 4 grid-nodes per wavelength, respectively. The grid cannot capture variations in heterogeneities smaller than the spacing, although waves in real media are sensitive to them up to a certain extent. Thus, it is very useful to determine the best-possible macroscopic values for subgrid-scale heterogeneities on the grid. Effective-medium (Backus, 1962; Schoenberg and Muir, 1989) or homogenization theory (Bensoussan et al., 1978) tells us how to define these macroscopic parameters. Effective or coarse representations of fine-scale model variations may have reduced symmetry, i.e., they contain extrinsic/layered anisotropy. In other words, a fine-scale layered isotropic medium is well described by an effective coarse-scale anisotropic medium (e.g., Backus, 1962). However, this also depends on the structure of the wave equation, e.g., upscaling the acoustic wavespeed in the simple acoustic wave equation does not result in lowered symmetry, as we will see in the forthcoming sections. There are a range of different upscaling methods, each based on a variety of assumptions since there are no optimal choices for the approximations. Without being exhaustive, we cite operator-based upscaling (Christie et al., 1996; Vdovina et al., 2005), the averaging of displacement-stress, displacement-energy or stress-energy relations(Zijl et al.,

---

* Tata Institute of Fundamental Research, Navy Nagar, Colaba, Mumbai-400005, India.

† CSIR-National Geophysical Research Institute, Uppal Road, Habsiguda, Hyderabad-500007, India.

‡ Shell Global Solutions International B.V., Grasweg 31, 1031 HW Amsterdam, The Netherlands.

E-mail: `ajaymalkoti@ngri.res.in` (corresponding author), `hanasoge@tifr.res.in`, `ReneEdouard.Plessix@shell.com`

2002; Grechka and Kachanov, 2006; Gao et al., 2015),homogenization theory (Moulinec and Suquet, 1998; Brisard and Dormieux, 2010; Capdeville et al., 2015; Cance and Capdeville, 2015; Burgos et al., 2016; Mishra et al., 2016; Song and Jordan, 2018), wavelet-based theory (Dorobantu and Engquist, 1998; Andersson et al., 1999; Persson and Runborg, 2001; Chertock and Levy, 2005; Coult, 2006; Engström and Sjöberg, 2007; De Leon, 2008; Engquist and Runborg, 2009), and Renormalization group (RG)-based theory (Hanasoge, 2016; Fichtner and Hanasoge, 2017; Hanasoge et al., 2017; Kennett and Fichtner, 2020). Those efforts have shown that even if one limits the analysis to the acoustic wave propagation, the effective, upscaled "acoustic" macroscopic parameters include the effects of some small-scale variations that can be of elastic nature. Here, we discuss an efficient implementation of RG theory with the acoustic wave equation.

Renormalization group theory aims at correcting the wave-equation parameters in such a way that the simulated waveform still includes the effects of the small-scale variations, despite a coarse discretization. In this method, the low-wavenumber part of the given model parameters, which can be adequately sampled by a coarse grid, is modified to account for the effects caused by the high-wavenumber variations that are only visible on a fine grid. RG-theory based upscaling requires multi-dimensional forward and inverse Fourier transforms to go back and forth between the spatial and wavenumber domains and involves inverting a large matrix when applied on the full computational domain (Hanasoge, 2016; Fichtner and Hanasoge, 2017). In realistic numerical applications, this can lead to a large computational overhead. In this work, we propose the RG-upscaling method based upon modified Fourier operator and domain decomposition. We divide the complete domain into several sub-domains in order to reduce the computational overhead and to allow for the possibility of a parallel implementation. However, a straightforward application of this upscaling in each sub-domain leads to edge effects caused by artificial discontinuities between the sub-domains. We then implement an "expansion and truncation" technique that allows overlapping between neighboring sub-domains and thus avoids those edge effects. This method differs from the overlapping domain decomposition technique.

The outline of the manuscript is as follows. In the first part, we apply RG theory to the 2D acoustic wave equation using modified Fourier operator. In the second section, we explain the how entire domain is decomposed into subdomains and expansion and truncation technique is applied for upscaling. Subsequently, we describe some numerical examples to evaluate the proposed approach, followed by a summary and conclusions.

## THEORY

We begin with the acoustic wave equation in the frequency (temporal-Fourier) domain,

$$-\omega^2 p(\omega, \boldsymbol{x}) = c^2(\boldsymbol{x}) \Delta p(\omega, \boldsymbol{x}) + s(\omega, \boldsymbol{x}), \qquad (1)$$

where $p$ and $s$ are the pressure field and the source function, respectively, $\Delta$ is the Laplace operator, $\boldsymbol{x}$ is the spatial coordinate, $\omega$ the angular frequency, and $c$ is the "acoustic" or compressional velocity.

The product, $q(\omega, \boldsymbol{x}) = c^2(\boldsymbol{x}) \Delta p(\omega, \boldsymbol{x})$, between the model parameter, $c(\boldsymbol{x})$, and the Laplacian of the pressure field, $\Delta p(\omega, \boldsymbol{x})$, in the spatial domain becomes a convolution in the wavenumber (spatial-Fourier) domain. Indeed, $\hat{q}(\omega, \mathbf{k}) = \int_{-\infty}^{\infty} \mathbf{k}^2 \hat{p}(\omega, \mathbf{k}) \hat{c}^2(\mathbf{k}' - \mathbf{k}) d\mathbf{k}'$, where $\mathbf{k}$ denotes the wavenumber, and the quantities with and without a hat sign are in the wavenumber domain and spatial domain, respectively. This convolution means that all the wavenumbers of the model parameter, $c^2$, affect the pressure wave's propagation up to a certain extent depending on the smoothness of the parameter's variations with respect to the wavelength. Therefore, one cannot fully isolate the response corresponding to only the low wavenumbers, i.e., the smooth component of the model parameter. Even when we are interested only in the low-frequency response, we theoretically need to solve the wave equation with a complete wavenumber representation of the seismic parameters, i.e., over a fine grid that captures the full range of parameter variations. In practice, this would be computationally very expensive. A typical remedy consists of calculating effective, macroscopic parameters while limiting errors arising from coarse-grid discretization.

To achieve this, we transform the wave equation (equation 1) into the wavenumber domain by applying the spatial Fourier operator, $\mathcal{F}$ (see appendix A). Since the Fourier operator is invertible ($\mathcal{F}^{-1}\mathcal{F} = \mathcal{F}\mathcal{F}^{-1} = I$, with $I$ the identity operator), we may rewrite equation 1 as follows:

$$-\omega^2 \mathcal{F}^{-1}\mathcal{F}p = \mathcal{F}^{-1}\mathcal{F}c^2\mathcal{F}^{-1}\mathcal{F}\Delta\mathcal{F}^{-1}\mathcal{F}p + \mathcal{F}^{-1}\mathcal{F}s. \quad (2)$$

We now define the following quantities in the wavenumber domain:

$$\begin{cases} \hat{p} = \mathcal{F}p; \\ \hat{s} = \mathcal{F}s; \\ \hat{C} = \mathcal{F}c^2\mathcal{F}^{-1}; \\ \hat{\Delta} = \mathcal{F}\Delta\mathcal{F}^{-1}. \end{cases} \qquad (3)$$

Multiplying equation 2 by $\mathcal{F}$, we obtain the wavenumber-domain acoustic wave equation

$$-\omega^2 \hat{p} = \hat{C}\hat{\Delta}\hat{p} + \hat{s}. \qquad (4)$$

Given an arbitrary user-prescribed, case-specific, cut-off wavenumber, we may decompose the spatial Fourier operator into two parts $\mathcal{F}_l$ and $\mathcal{F}_h$, yielding the low-wavenumber and high-wavenumber parts, respectively (see Appendix

A). In this manner, pressure and source terms can be written as,

$$\hat{p} = \begin{pmatrix} \hat{p}_l \\ \hat{p}_h \end{pmatrix} = \begin{pmatrix} \mathcal{F}_l\, p \\ \mathcal{F}_h\, p \end{pmatrix}; \quad \hat{s} = \begin{pmatrix} \hat{s}_l \\ \hat{s}_h \end{pmatrix} = \begin{pmatrix} \mathcal{F}_l\, s \\ \mathcal{F}_h\, s \end{pmatrix}.$$

(5)

where the operator containing the parameters $\hat{C}$ is

$$\hat{C} = \begin{pmatrix} \mathcal{F}_l \\ \mathcal{F}_h \end{pmatrix} c^2 \begin{pmatrix} \mathcal{F}_l^{-1} & \mathcal{F}_h^{-1} \end{pmatrix} = \begin{pmatrix} \mathcal{F}_l\, c^2 \mathcal{F}_l^{-1} & \mathcal{F}_l c^2 \mathcal{F}_h^{-1} \\ \mathcal{F}_h c^2 \mathcal{F}_l^{-1} & \mathcal{F}_h c^2 \mathcal{F}_h^{-1} \end{pmatrix}$$
$$= \begin{pmatrix} \hat{C}_{ll} & \hat{C}_{lh} \\ \hat{C}_{hl} & \hat{C}_{hh} \end{pmatrix},$$

(6)

and the derivative operator, $\hat{\Delta}$, is

$$\hat{\Delta} = \begin{pmatrix} \mathcal{F}_l \\ \mathcal{F}_h \end{pmatrix} \Delta \begin{pmatrix} \mathcal{F}_l^{-1} & \mathcal{F}_h^{-1} \end{pmatrix} = \begin{pmatrix} \hat{\Delta}_{ll} & 0 \\ 0 & \hat{\Delta}_{hh} \end{pmatrix}.$$

(7)

With these definitions, we obtain the following system of equations governing $\hat{p}_l$ and $\hat{p}_h$:

$$\begin{cases} -\omega^2 \hat{p}_l = \hat{C}_{ll}\, \hat{\Delta}_{ll}\, \hat{p}_l + \hat{C}_{lh}\, \hat{\Delta}_{hh}\, \hat{p}_h + \hat{s}_l, \\ -\omega^2 \hat{p}_h = \hat{C}_{hl}\, \hat{\Delta}_{ll}\, \hat{p}_l + \hat{C}_{hh}\, \hat{\Delta}_{hh}\, \hat{p}_h + \hat{s}_h. \end{cases}$$

(8)

Equations for $\hat{p}_l$ and $\hat{p}_h$ are coupled, as expected, because the spatial-domain product between model parameters and derivatives of the pressure corresponds to a convolution in the wavenumber (spatial-Fourier) domain. The second part of equation 8 gives:

$$\hat{p}_h = -\left(\omega^2 + \hat{C}_{hh}\hat{\Delta}_{hh}\right)^{-1} \hat{C}_{hl}\hat{\Delta}_{ll}\hat{p}_l - \left(\omega^2 + \hat{C}_{hh}\hat{\Delta}_{hh}\right)^{-1} \hat{s}_h.$$

(9)

Using this expression to eliminate $\hat{p}_h$ in the first part of the equation 8, we arrive at the equation for the pressure field in the low-wavenumber regime, $\hat{p}_l$,

$$-\omega^2 \hat{p}_l = \left[\hat{C}_{ll} - \hat{C}_{lh}\hat{\Delta}_{hh}\left(\omega^2 + \hat{C}_{hh}\hat{\Delta}_{hh}\right)^{-1} \hat{C}_{hl}\right] \hat{\Delta}_{ll}\hat{p}_l$$
$$+ \hat{s}_l - \hat{C}_{lh}\hat{\Delta}_{hh}\left(\omega^2 + \hat{C}_{hh}\hat{\Delta}_{hh}\right)^{-1} \hat{s}_h.$$

(10)

Defining

$$\begin{cases} \hat{C}_E(\omega) = \left[\hat{C}_{ll} - \hat{C}_{lh}\hat{\Delta}_{hh}\left(\omega^2 + \hat{C}_{hh}\hat{\Delta}_{hh}\right)^{-1} \hat{C}_{hl}\right], \\ \hat{s}_E(\omega) = \hat{s}_l - \hat{C}_{lh}\hat{\Delta}_{hh}\left(\omega^2 + \hat{C}_{hh}\hat{\Delta}_{hh}\right)^{-1} \hat{s}_h, \end{cases}$$

(11)

We obtain the following equation for $\hat{p}_l$

$$-\omega^2 \hat{p}_l = \hat{C}_E(\omega)\hat{\Delta}_{ll}\hat{p}_l + \hat{s}_E(\omega).$$

(12)

To transform equation 12 back to the spatial domain, we first rewrite it by equating the identity with the product of the Fourier with its inverse:

$$-\omega^2 \mathcal{F}_l\mathcal{F}_l^{-1}\hat{p}_l = \mathcal{F}_l\mathcal{F}_l^{-1}\hat{C}_E(\omega)\mathcal{F}_l\mathcal{F}_l^{-1}\hat{\Delta}_{ll}\mathcal{F}_l\mathcal{F}_l^{-1}\hat{p}_l + \mathcal{F}_l\mathcal{F}_l^{-1}\hat{s}_E(\omega)$$

(13)

Then by introducing:

$$\begin{cases} C_E = \mathcal{F}_l^{-1}\hat{C}_E(\omega)\mathcal{F}_l, \\ \Delta_{ll} = \mathcal{F}_l^{-1}\hat{\Delta}_{ll}\mathcal{F}_l, \\ s_E = \mathcal{F}_l^{-1}\hat{s}_E(\omega), \end{cases}$$

(14)

and multiplying equation 13 by $\mathcal{F}_l^{-1}$, we obtain with $p_l = \mathcal{F}_l^{-1}\hat{p}_l$:

$$-\omega^2 p_l = C_E(\omega)\Delta_{ll}p_l + s_E(\omega).$$

(15)

The equation 12 is not the standard wave equation since the model parameter operator, $\hat{C}_E$, depends on frequency. Thus, within this framework, upscaling leads to frequency-dependent parameters. To obtain a pure acoustic wave equation, we further simplify the approach by fixing the angular frequency in $C_E$ and $s_E$ to $\omega = \omega_0$. The reference angular frequency, $\omega_0$, could be a representative value within the frequency band of the seismic experiment. If we assume $\omega^2\hat{\Delta}_{hh}^{-1} << \hat{C}_{hh}$, we can choose $\omega_0 = 0$ and $\hat{C}_E$ simplifies to:

$$\hat{C}_E \simeq \left[\hat{C}_{ll} - \hat{C}_{lh}\hat{C}_{hh}^{-1}\hat{C}_{hl}\right].$$

(16)

With this approximation, $\hat{C}_E$ (and similarly $\hat{s}_E$) becomes frequency independent and equation 13 reduces to a standard acoustic wave equation. The term $\hat{C}_{ll}$, in equation 16 simply represents the low-wavenumber part for the complete domain, which is equivalent to the apodization of undesired spatial wavenumbers. The remaining part $\hat{C}_{lh}\hat{C}_{hh}^{-1}\hat{C}_{hl}$, known as the correction term, arises due to the effect of high wavenumbers. With the acoustic wave equation, the low-frequency component of the Fourier-derivative operator emerges from Renormalization group theory, i.e., $\Delta_{ll} = \mathcal{F}_l^{-1}\hat{\Delta}_{ll}\mathcal{F}_l$. An important caveat is that this is not true for general derivative operators, where density or tensor coefficients need to be considered (Hanasoge, 2016; Fichtner and Hanasoge, 2017). Invoking scale separation and dropping the temporal-frequency dependency in the effective wave speed equation yields nearly identical results, i.e., tests performed with and without constant frequency term (i.e., $\omega = 0$) in equation 12 produce the same answers for low frequencies.

## NUMERICAL IMPLEMENTATION

The finite-difference solution of wave equation demands minimum numerical-dispersion error by constraining the grid spacing, $\Delta h < \lambda_{\min}/n$, where $\lambda_{\min}$ is the smallest wavelength traveling in the medium, and $n$ is the number of grid points per wavelength. The numerical scheme of order, $\mathcal{O}(\Delta t^2, \Delta^4)$, requires $\lambda_{\min}$ to be sampled by at least eight grid nodes. The above criteria are independent of the variations in the model parameters. However, a highly heterogeneous model may require sampling it with a very fine grid spacing (up to Nyquist frequency); otherwise, any high-wavenumber variations present in the model are lost. The fine sampling rate is much higher than the one prescribed by the dispersion criteria, and it results in greatly

increased computational cost. This in turn, also controls the time step ($\Delta t$) by virtue of the Courant condition. Therefore, we would like to upscale this fine-scale model to a coarser model with grid spacing as demanded by dispersion criteria or as close as possible while preserving the wave characteristics and reduce its computational cost.

Let us assume a computational domain with lengths $L_x$ and $L_z$ along the $x$ and $z$ directions, respectively, and discretized with uniform spacing, $\Delta h_f$, along both axes (Figure 1a). Here subscript $f$ refers to the fine-sampled model. The fine grid contains $N_{xf} \times N_{zf}$ number of nodes, where, $N_{xf} = \left\lfloor \dfrac{L_x}{\Delta h_f} \right\rfloor + 1$, $N_{zf} = \left\lfloor \dfrac{L_z}{\Delta h_f} \right\rfloor + 1$, and $\lfloor \cdot \rfloor$ here represents the floor function. This model can be upscaled using the proposed RG-theory-based upscaling technique in several ways. The most straightforward way is to consider the entire model and upscaling it will yield the parameter model consisting of $N_{xc} \times N_{zc}$ number of nodes with a grid spacing $\Delta h_c$ (Figure 1a) and here, $N_{xc} = \left\lfloor \dfrac{L_x}{\Delta h_c} \right\rfloor + 1$, $N_{zc} = \left\lfloor \dfrac{L_z}{\Delta h_c} \right\rfloor + 1$. This strategy was adopted by Fichtner and Hanasoge (2017) with the 1D-wave equation. However, it is very challenging to extend this approach to higher dimensions because the computational cost of the scheme rises sharply with domain size, as it involves storing and inverting the a very large size Fourier matrix (see $\hat{C}_{hh}$ term in equation 16). For example, for 1D-domain having $N-$nodes and 2D-domain with $N \times N$ nodes, the Fourier matrices are of size $N^2$ and $N^4$, respectively. Further, the computational complexity for inverting a matrix of size $N \times N$ is given by $O(N^a)$ where $2.73 < a < 3$, depending upon the algorithm used for the inversion (Coppersmith and Winograd, 1987).

To reduce the size of the Fourier transform, we first decompose the whole domain into sub-domains of lengths $L'_x$ and $L'_z$ (as in Hanasoge et al., 2017), as shown in Figure 1b. This gives $\dfrac{L_x}{L'_x} \times \dfrac{L_z}{L'_z}$ number of sub-domains. Each sub-domain contains $N'_{xf} \times N'_{zf}$ number of grid nodes at the fine discretization level and $N'_{xc} \times N'_{xc}$ grid nodes at the coarse discretization level (upscaled model). Here, we require the number of nodes in the fine grid of the subdomain in each direction to be an integer multiple of the number of nodes in the coarse grid. The final RG-upscaled model is obtained by joining all upscaled subdomains. For the wave upscaling problem, we observed some edge effects in the final upscaled parameter model, which introduces artificial discontinuities at the edges, as shown in Figure 2. Our attempts to mitigate this effect using some well-known techniques of applying a taper (e.g., Hann or Tukey window) led to instabilities in the solver.

The edge effect can be avoided using the "expansion and truncation" technique with overlapping (Figure 1c). In this technique, the model is expanded with a few additional layers of nodes around the domain (to be upscaled). After upscaling the expanded domain, the additional node layers should be removed or truncated to get the exact upscaled subdomain. The additional node layers create an overlap region which helps in maintaining the continuity. This overlap region should be large enough to avoid the artifacts but small enough to not add appreciably to the computation cost. To begin with this method, we first choose the size of the subdomain along any axis ($L''$) based on the classical Rayleigh's limit for resolution, which states that two events cannot be resolved by a wave if their separation is less than a quarter of wavelength. Based upon this, we can choose the size of the subdomain as– $\min(L''_x, L''_z) > \dfrac{\lambda_{\min}}{4}$, where, $\lambda_{\min}$ is the smallest wavelength traveling in the medium. Then we define the coarsening ratio or decimation level, $\sigma$, as the ratio of the number of nodes in a given subdomain to that of an upscaled domain. For simplicity's sake, we consider only power-of-two ratios: $\sigma_x = N''_{xf}/N''_{xc} = 2^i$ and $\sigma_z = N''_{zf}/N''_{zc} = 2^j$ (for integers $i$ and $j$). Without expansion, the application of upscaling independently on each sub-domain generates edge effects over $q_x$ and $q_z$ node layers around the edges of the sub-domains, as observed in the upscaled model (Figure 2b). In the present analysis, we use $q_x = q_z = 4$ for all cases. We expand each subdomain with $p_x = \sigma_x q_x$ nodes on both sides of the $x-$direction and $p_z = \sigma_z q_z$ nodes on both sides of the $z-$direction. This means that the expanded sub-domain has $(N''_{xf} + 2p_x) \times (N''_{zf} + 2p_z)$ grid nodes at the fine discretization and $(N''_{xc} + 2q_x) \times (N''_{zc} + 2q_z)$ grid nodes after upscaling with the coarse discretization. We then truncate the upscaled domain by removing the additional nodes ($q_x$ and $q_z$) arising due to the expansion around the subdomain. This complete process, termed as expansion and truncation of subdomains, is shown in Figure 3.

The method requires some adaptations for the sub-domains situated at the edges or corners of the model where expansion in some directions is not possible. In this situation, we can artificially extend the domain with a simple extrapolation scheme or ignore the expansion where it is not possible.

## NUMERICAL RESULTS

We apply different upscaling approaches to each fine-scale reference model (termed REF) in order to assess the relative performance of the RG-theory-based method.

- *Arithmetic or harmonic averaging*: The model parameter on the coarse grid is obtained by averaging over the values on the fine grid,
$M_{kl} = \displaystyle\sum_{i=k\sigma_x}^{(k+1)\sigma_x-1} \sum_{j=l\sigma_z}^{(l+1)\sigma_z-1} w_{ij} m_{ij}$, where $M_{kl}$ are the values defined on the coarse grid, $m_{ij}$ is the material parameter to be averaged on the fine grid and $w_i$ represents weights such that their sum is unity. In the present case, we used $w_{ij} = \frac{1}{\sigma_x \sigma_z}$ and averaging was carried out on the inverse of wave speed since it better preserves the travel time. Models upscaled with this method are termed as "Upscaled Average" (UAV).
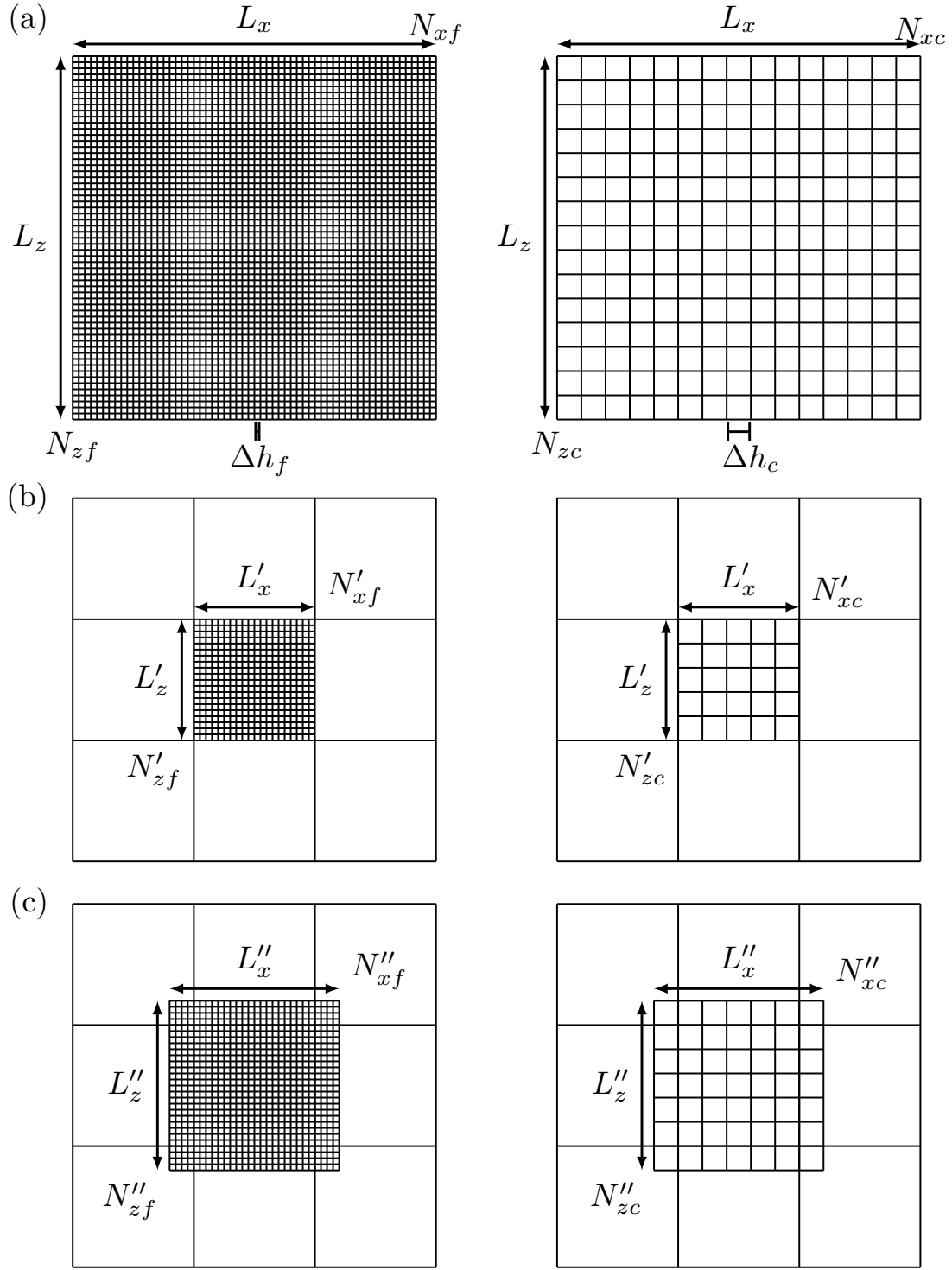
Figure 1: The figure demonstrates upscaling the given fine-sampled model (left column) to a coarse-upscaled model (right column) using the RG theory based technique, which is possible in three ways. First is shown in (a) where the complete domain is taken as such and upscaled to yield a coarse model. Second is shown in (b) when the domain is decomposed into several subdomains and then each subdomain is upscaled individually and independently. Later, all upscaled subdomains are stitch together to yield the complete upscaled-coarse model. Third, Expansion and truncation technique is shown in (c). In this technique the selected subdomain is first expanded with a few additional nodes and upscaled, which also contains additional nodes. The desired upscaled part is extracted by truncating the additional nodes. The additional nodes around the upscaled-subdomains overlaps with neighboring subdomains which maintain the continuity.
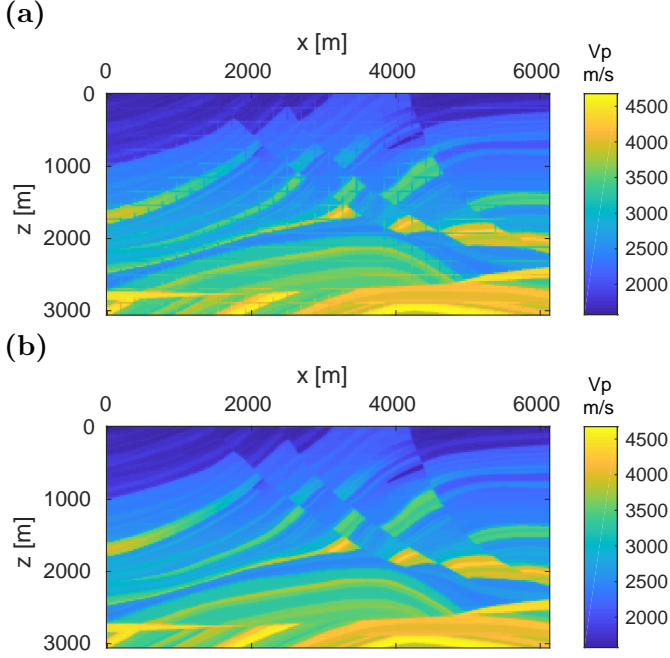
**(a)**



**(b)**



Figure 2: (a) The edge effect for the Marmousi model when it is upscaled using a block of size $N_f^x \times N_f^z$, each of which is directly upscaled on to a block of size $N_c^x \times N_c^z$. (b) The upscaled Marmousi model with the expansion and truncation technique.

- *Wavenumber-domain filtering using Gaussian window*: The model parameter is transformed into the wavenumber domain and low-pass filtered using a Gaussian, $w(k) = \exp\left(-\frac{k^2}{4D^2}\right)$ for $|k| \leq k_0$ and 0 otherwise, where $k = \sqrt{k_x^2 + k_z^2}$ and $k_x$ and $k_z$ are wavenumbers along the x and z directions, respectively, $k_0 = \frac{2\pi}{\lambda_0}$ is the wavenumber corresponding to the user-prescribed threshold value of wavelength, $\lambda_0$, and $D$ ia a parameter that controls the slope of the Gaussian curve. Finally, the values on the coarse grid are obtained with the inverse Fourier transform. Models upscaled using this method are termed as "Upscaled Gaussian filtered" (UFG).

- *Renormalization group theory*: The parameters on the coarse grid are obtained using the approach described above with reference angular frequency, $\omega_0 = 0$. Models upscaled using this method are termed as "Upscaled RG" (URG).

To demonstrate the application of the RG-upscaling, we will use different models (presented later in this section) and different geometries, namely, transmission and reflection geometry. The above three upscaling methods will be applied to each model and compared for their performance.
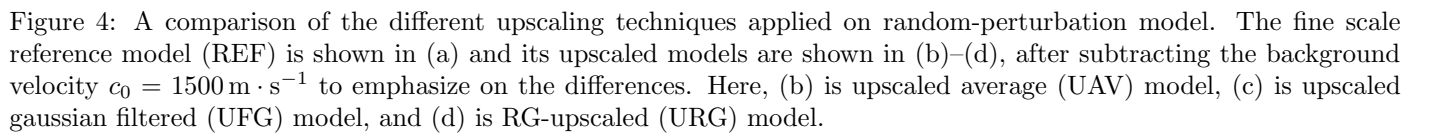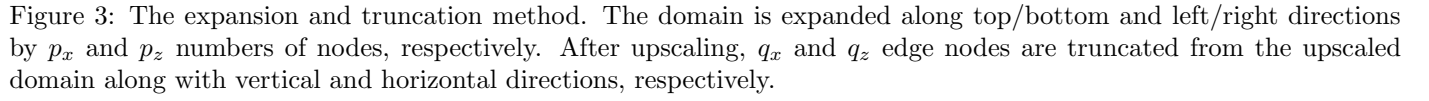
**Transmission geometry**

In the transmission case example, we consider REF model consisting of 1024×512 nodes. The source and receiver are located at the same depth near left $((x, z) = d_f(42, 258))$ and right $((x, z) = d_f(986, 258))$ edges of model, respectively. The fine grid representation corresponds to a spacing of $d_f = 1.5$ m and with an upscaling of $\sigma = 4$, the coarse spacing is $d_c = 6$ m. Absorbing conditions are applied at all boundaries for transmission geometry. We use the broadband Ricker wavelet of central frequency $f_0$ which shows a good frequency response up to 1.645 $f_0$ (Wang, 2015). We have performed simulations for various values of $f_0$ (= 5, 10, 15, and 20 Hz) for which the maximum frequency of response are $f_{max}$ = 8.22, 16.45, 24.67, and 32.9 Hz, respectively. For the given source-receiver distance, and the average velocity of 1500 m · s$^{-1}$ (least value for all models), seismic waves propagate approximately 5 wavelengths and 31 wavelengths at central frequencies $f_0$ = 5 and 20 Hz, respectively. The numerical wave simulation is carried out using a fourth-order finite-difference scheme with vectorization (Malkoti et al., 2018; Li et al., 2021). We note that the 6 m spacing corresponds to about one-tenth of the wavelength at 24.64 Hz (the maximum frequency of the 15 Hz Ricker wavelet approximately).

*Model with random perturbations*

The reference velocity model in this case is described by $c(x, z) = c_0 + \Delta c(x, z)$, where the model has a uniform background p-wave velocity of $c_0 = 1500$ m · s$^{-1}$ and $\Delta c$ is a uniform-random variable with a maximum permissible amplitude of 20 percent of $c_0$ value. In Figure 4, we show the reference (REF) and upscaled models (UAV, UFG, URG); the value $c_0$ has been subtracted. The difference plot reveals that the UFG model differs least from $c_0$, followed by URG and the largest deviations for the UAV model. As evident from the figure, only the UAV and URG models could preserve the high-frequency characteristics. How these characteristics in upscaled models affect the kinematic and dynamic features of the seismogram is shown in Figure 5.

The synthetic seismogram obtained for the fine-scale model is marked as reference (REF). At the low-frequency end of our analysis, 5 Hz, all models produce nearly identical seismograms. However, as the source frequency increases (up to 15 Hz), there is an onset of traveltime error in all cases and the error is relatively large for the UFG model. At higher frequencies, all waveforms show significant errors in both amplitude and traveltime. At the highest frequencies, the performance of the RG-theory-based upscaling is roughly equivalent to that of an averaging method.
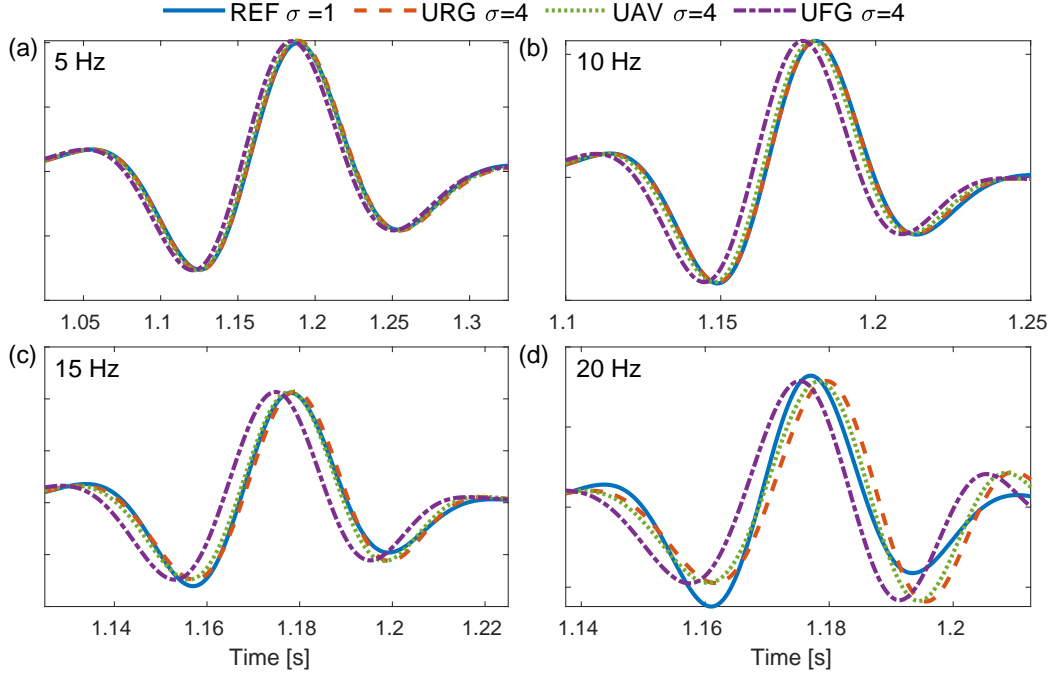
Figure 3: The expansion and truncation method. The domain is expanded along top/bottom and left/right directions by $p_x$ and $p_z$ numbers of nodes, respectively. After upscaling, $q_x$ and $q_z$ edge nodes are truncated from the upscaled domain along with vertical and horizontal directions, respectively.



Figure 4: A comparison of the different upscaling techniques applied on random-perturbation model. The fine scale reference model (REF) is shown in (a) and its upscaled models are shown in (b)–(d), after subtracting the background velocity $c_0 = 1500\,\mathrm{m \cdot s^{-1}}$ to emphasize on the differences. Here, (b) is upscaled average (UAV) model, (c) is upscaled gaussian filtered (UFG) model, and (d) is RG-upscaled (URG) model.

Figure 5: All traces in each subplot are obtained for the random model using the same source frequency (top-left). These are compared between the reference (REF) model and upscaled models (URG, UAV, UFG). Here, the decimation level, $\sigma$, represents the ratio of the number of nodes in a given subdomain to that in the upscaled domain.
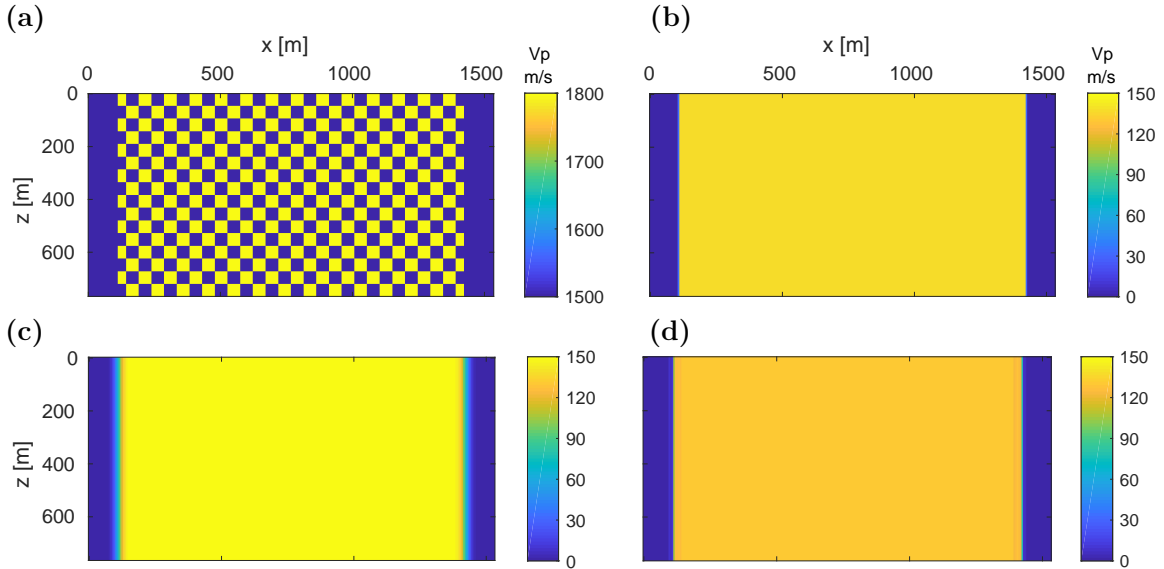


Figure 6: A comparison of different upscaling techniques applied on periodic model. The fine-scale reference model (REF) is shown in (a) and its checkerboard pattern is magnified for better visualization. The upscaled models difference from their background velocity $c_0 = 1500 \, \mathrm{m \cdot s^{-1}}$ is shown in subplot– (b) the upscaled average (UAV) model, (c) upscaled gaussian filtered (UFG) model, and (d) RG-upscaled (URG) model.

*Model with periodic perturbations*

A reference periodic model (Figure 6) is generated using a checkerboard grid, where the $c_0 = 1500\,\text{m}\cdot\text{s}^{-1}$ and $\Delta c$ represents periodic fluctuation between $0 - 300\,\text{m}\cdot\text{s}^{-1}$ with a periodicity of $3\,\text{m}$. The model size and the fine grid spacing are the same as for the previous model (i.e., random model). As for the random model, we plot the REF and upscaled models with subtracted $c_0 = 1500\,\text{m}\cdot\text{s}^{-1}$ which is related to plotting only. The upscaled medium velocity is highest for UFG while the other two models, UAV and URG, are very close. The traces generated for the REF and upscaled media are shown in Figure 7. For this model as well, we observe, as expected, small errors at low frequencies, with increasing errors in all upscaled models at higher frequencies (up to $15\,\text{Hz}$) and the appearance of amplitude errors at the highest frequencies. It is worth noting that the waveforms computed using the UAV model show significant traveltime errors at frequencies of 10-20 Hz, phase delays are observed for the URG at high frequencies, whereas the phases are advanced for UAV and UFG.

## Reflection geometry

We used a model comprising three layers, with small-scale heterogeneities present in the second layer. The velocities for the layers are $[1500, 1600, 1800]\,\text{m}\cdot\text{s}^{-1}$, in depth-increasing order, as shown in Figure 8. The middle-layer in the model has a constant thickness of $300\,\text{m}$, which contains two types of heterogeneities, of dimensions $(1.5\,\text{m} \times 1.5\,\text{m})$ and $(7.5\,\text{m} \times 1.5\,\text{m})$, respectively. The heterogeneities are randomly distributed within the domain and have a finite probability of touching neighboring heterogeneities. Rectangular and square heterogeneities are assigned constant velocities of $2250\,\text{m}\cdot\text{s}^{-1}$ and $2200\,\text{m}\cdot\text{s}^{-1}$, respectively. We have used 19 shots, placed at the surface and at an interval of 40 nodes. Receivers are located at all nodes at the surface (in all the shots). We use a Ricker wavelet with a central frequency of $15\,\text{Hz}$. A comparison of seismograms is presented in Figure 9 for a single shot. The seismogram generated for URG is in good agreement with the waveform obtained for REF. Direct arrivals have been clipped in order to highlight the reflected phases. The reflected waveforms obtained using URG are slightly delayed in comparison to REF.

These two models are used for comparing the effect of upscaling in reverse time migration or RTM Baysal et al. (1983). It is widely used to generate kinematically accurate subsurface images by cross-correlating the forward and reverse propagating wavefields. The imaging condition used for RTM can be stated as,

$$I(x,z) = \sum_s \sum_\tau F(x,z,\tau) R(x,z,\tau), \qquad (17)$$

where $F(x,z,\tau)$ is the forward propagating source wavefield, $R(x,z,\tau)$ is the reverse propagating receiver wave-

field at time $\tau$, and $s$ represents sources/shots.

To carry out the comparison, we first compute the record for 19 shots using the reference model. We then compute the RTM images using these data for both the REF and the URG models. The RTM images thus obtained, shown in Figure 10, are nearly identical and show negligible shifts in reflector positions. In this process, we removed the direct arrivals before carrying out the RTM and applied a scaling to enhance the deeper reflector.

## COMPUTATION TIME

The REF model consisted of $1024 \times 512$ nodes, and the wave equation is solved for 4000-time steps. The total time taken for a single forward simulation on the REF model is $T_s \simeq 116\,\text{s}$ and time for carrying out RTM using single shot $T_r = 386\,\text{s}$. The computational cost of RTM is higher since it includes time for two forward calculations, cross-correlation of forward and adjoint wavefields, and I/O from storage.

The simulation time for the upscaled model consists of two parts- first, time spent in upscaling ($t_u$), and second, time spent in seismic simulation ($t_s$). Since the upscaling is an "embarrassingly parallel" problem, we can write its total cost as $t_u/N + t_s$, where $N$ is the number of cores used for parallelization. We carried out upscaling using $\sigma = 4$, which takes about $t_u = 35\,\text{s}$ (estimated for parallel execution) and $t_s = 6\,\text{s}$. The computation time for RTM using single-shot takes about $t_r = 29\,\text{s}$, which is almost 6-times faster. In fact, with increasing numbers of shots ($N_s$), the speedup obtained is even higher, approaching the ratio $T_r/t_r \sim 13$, for a large $N$,

$$\text{Speedup} = \frac{N_s \times T_r}{t_u/N + N_s \times t_r} = \frac{T_r}{t_u/(N \times N_s) + t_r} \to \frac{T_r}{t_r}. \tag{18}$$

Upscaling and RTM processes may be seen as the offline and online stages, respectively. The offline stage cost is high but it helps the online stage to run very efficiently and in the present case, the overall efficiency increases nearly 13 times.

## CONCLUSIONS

We have demonstrated the upscaling of the two-dimensional acoustic wave equation based on RG theory. This requires a modified 2D Fourier operator, decomposing the computational domain into subdomains for avoiding large-size multi-dimensional Fourier operators, and an "expansion and truncation" technique to mitigate edge effects along the edges of subdomains. We discuss various important characteristics for this scheme, e.g., it honors the wave equation, it is independent of the geometry of the heterogeneity or the layer structure present within the medium, it is free from boundary artifacts, and it does not lower the symmetry of the acoustic wave equation (for the density-invariant case). It is shown that the limit to which upscaling may be carried out is controlled by the property
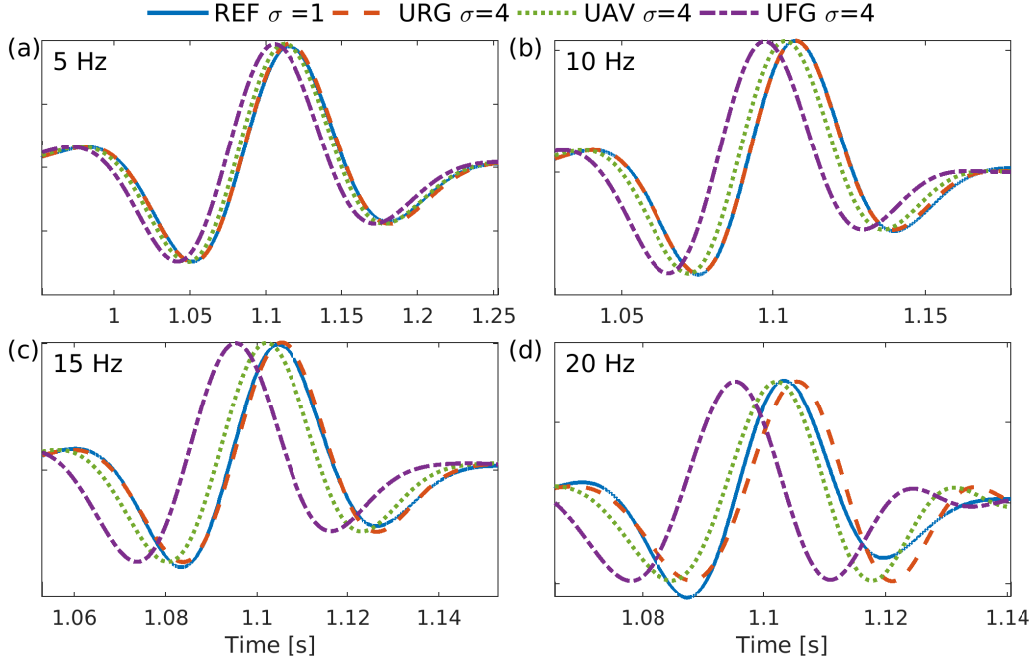
Figure 7: A comparison of traces is obtained for the reference periodic model (REF) and other upscaled models (UAV, UFG, and URG). All traces in each subfigure are generated using the same source frequency, shown on the top-left corner of each of the panels. Here, the decimation level, $\sigma$, represents the ratio of the number of nodes in a given subdomain to that in the upscaled domain.
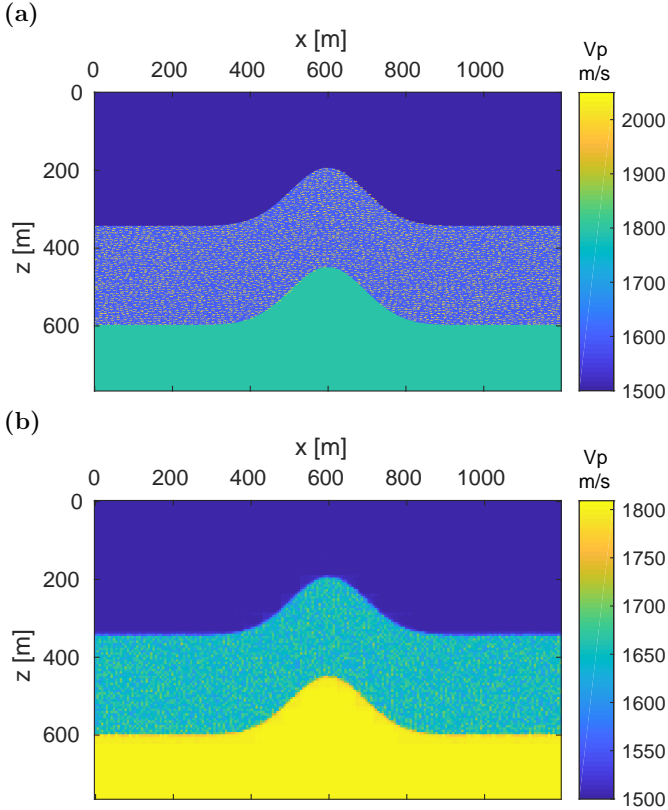


Figure 8: (a) The fine scale three-layered model with scatterers used as reference model (REF), and (b) the RG-upscaled model (URG).

of the numerical-derivative operator, i.e., accuracy and dispersion. We compare the seismograms computed post RG-based upscaling, harmonic averaging and low-pass filtering. This method reduces the computational cost significantly and makes the upscaling process feasible, even on computer systems with small memory size. At present, the technique has two limitations: 1) it relies on a uniform grid in order to apply Fourier-based upscaling and blocking process, 2) the determination of the $C_H$ term requires computing the inverse of a matrix (for each block), requiring large computation time, which in turn places constraints on the block size.

### APPENDIX A
### MODIFIED FOURIER OPERATOR

Consider a 2D function, $g(z, x)$, sampled uniformly over a 2D domain using $M \times N$ nodes as $g(i, j) = g(i\Delta h, j\Delta h)$ where $i \in \{1, 2, \ldots, N\}$ and $j \in \{1, 2, \ldots, M\}$. The conventional 2D-Fourier transform for this discrete function is given by $G(u, v) = \mathcal{F}g(i, j)$, and for the discrete case,
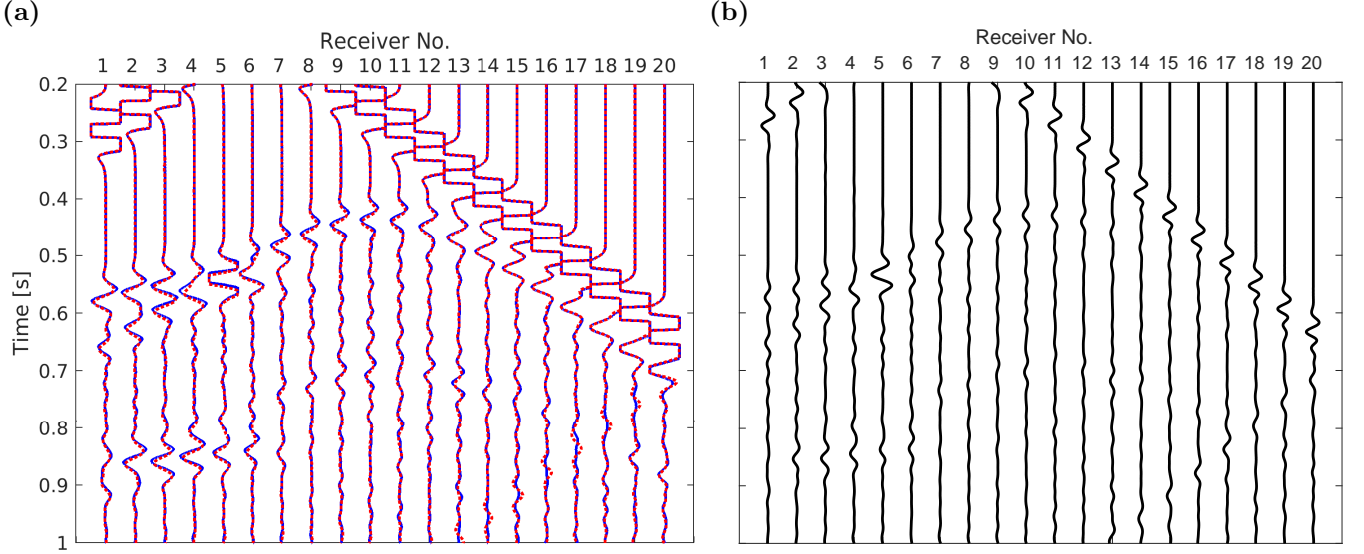
**(a)**



**(b)**

Figure 9: (a) A comparison of the seismogram obtained for three layer model with scatterers reference model (solid-blue line) and its RG upscaled model (dotted red line). (b) The difference between these two seismograms at the common receivers locations.
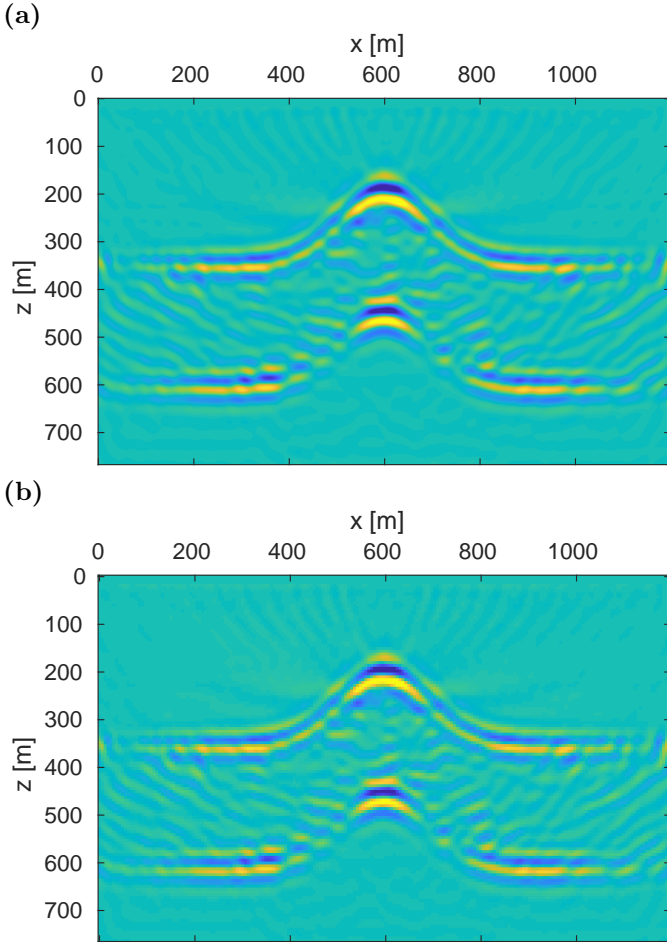
**(a)**



**(b)**



Figure 10: A comparison of RTM images obtained for three layered model with scatterers using– (a) fine scale reference model (REF) and (b) upscaled model (URG).

it may be represented as

$$G_{u,v} = \sum_{m=0}^{M-1} \sum_{n=0}^{N-1} e^{-2\iota\pi(ui/M + vj/N)} g_{i,j} \,, \qquad \text{(A-1)}$$

and in matrix form as (Van Loan, 1992),

$$\boldsymbol{G} = \boldsymbol{F}\boldsymbol{g}. \qquad \text{(A-2)}$$

We will modify the Fourier operator $\boldsymbol{F}$ such that it yields the response to high and low-wavenumbers separately. First, we look into the 2D wavenumber spectrum, $\boldsymbol{K}(u,v)$ in Figure 11, and mark the regions for low and high discrete-wavenumber. Here the lower $K$ and $L$ wavenumbers (user prescribed) represent the lower wavenumbers. It will pro-duce into four wavenumber-based regions— low-low ($\boldsymbol{K}_{\bullet,l}^{\bullet} \boldsymbol{K}_{\bullet,l}^{\bullet}$), low-high ($\boldsymbol{K}_{\bullet,l}^{\bullet} \boldsymbol{K}_{\bullet,h}^{\bullet}$), high-low ($\boldsymbol{K}_{\bullet,h}^{\bullet} \boldsymbol{K}_{\bullet,l}^{\bullet}$), high-high ($\boldsymbol{K}_{\bullet,h}^{\bullet} \boldsymbol{K}_{\bullet,h}^{\bullet}$). The dot ($\bullet$) in the subscript represents the axis, and the superscript denotes the positive/negative wavenumbers. A combination of wavenumber (positive/negative) and the selected axis ($u/v$) further divides each aforementioned region, e.g., low-low regions, into four parts. The four wavenumber-based regions are extracted out as shown in Figure 12, and the corresponding rows of the operator for each region are obtained as— $\boldsymbol{F}_{ll}, \boldsymbol{F}_{lh}, \boldsymbol{F}_{hl}, \boldsymbol{F}_{hh}$. These four operators are be concatenated to form the modified Fourier operator (on the right) and maybe succinctly rep-resented (on the left) as—

$$\begin{bmatrix} \mathcal{F}_l \\ \mathcal{F}_h \end{bmatrix} = \begin{bmatrix} \boldsymbol{F}_{ll} \\ \boldsymbol{F}_{lh} \\ \boldsymbol{F}_{hl} \\ \boldsymbol{F}_{hh} \end{bmatrix}. \qquad \text{(A-3)}$$

In this modified Fourier operator, the first $KL$ rows will correspond to the lower wavenumbers and the rest $MN-$
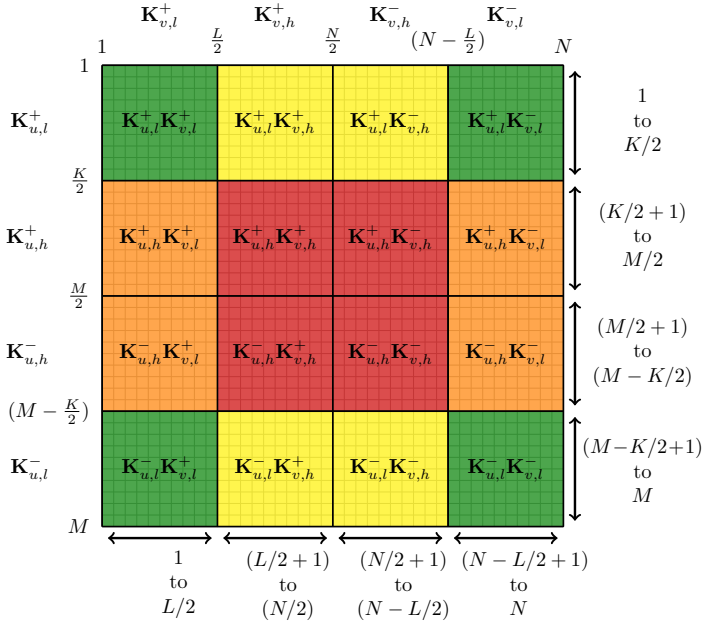
Figure 11: Distribution of wavenumbers ($\boldsymbol{K}(u,v)$) obtained for the conventional Fourier transform $G(u,v) = \boldsymbol{F}g(x,z)$. The total number of discrete wavenumbers along the $u,v$ axes are $M, N$, of which only the lower $K$ and $L$ wavenumberss along the respective axes are to be retained. Subscripts $u$ and $v$ are used to indicate the associated axes, and $h$, $l$ represent the high and low wavenumber ranges. Superscripts $+, -$ indicate positive and negative wavenumbers.

$KL$ rows to higher wavenumbers. Once the operator is constructed, then the computation of the expression is straightforward.

$$\hat{C}_{ll} = \mathcal{F}_l c^2 \mathcal{F}_l \qquad (A\text{-}4)$$

$$\hat{C}_{lh} = \mathcal{F}_l c^2 \mathcal{F}_h \qquad (A\text{-}5)$$

$$\hat{C}_{hl} = \mathcal{F}_h c^2 \mathcal{F}_l \qquad (A\text{-}6)$$

$$\hat{C}_{hh} = \mathcal{F}_h c^2 \mathcal{F}_h \qquad (A\text{-}7)$$

Here $c$ is the velocity of the medium, expressed as a diagonal matrix.

## REFERENCES

Andersson, U., B. Engquist, G. Ledfelt, and O. Runborg, 1999, A Contribution to Wavelet-Based Subgrid Modeling: Applied and Computational Harmonic Analysis, **7**, 151–164.

Backus, G. E., 1962, Long-wave elastic anisotropy produced by horizontal layering: Journal of Geophysical Research, **67**, 4427–4440.

Baysal, E., D. D. Kosloff, and J. W. Sherwood, 1983, Reverse time migration: GEOPHYSICS, **48**, 1514–1524.

Bensoussan, A., J. Lions, and G. Papanicolaou, 1978, Asymptotic Analysis for Periodic Structures, 1 ed.: North Holland.

Brisard, S., and L. Dormieux, 2010, FFT-based methods for the mechanics of composites: A general variational framework: Computational Materials Science, **49**, 663–671.

Burgos, G., Y. Capdeville, and L. Guillot, 2016, Homogenized moment tensor and the effect of near-field heterogeneities on nonisotropic radiation in nuclear explosion: Journal of Geophysical Research: Solid Earth, **121**, 4366–4389.

Cance, P., and Y. Capdeville, 2015, Validity of the acoustic approximation for elastic waves in heterogeneous media: GEOPHYSICS, **80**, T161–T173.

Capdeville, Y., M. Zhao, and P. Cupillard, 2015, Fast Fourier homogenization for elastic wave propagation in complex media: Wave Motion, **54**, 170–186.

Chertock, A., and D. Levy, 2005, On Wavelet-Based Numerical Homogenization: Multiscale Modeling & Simulation, **3**, 65–88.

Christie, M. A., et al., 1996, Upscaling for reservoir simulation: Journal of petroleum technology, **48**, 1–004.

Coppersmith, D., and S. Winograd, 1987, Matrix multiplication via arithmetic progressions: Proceedings of the nineteenth annual ACM symposium on Theory of computing, 1–6.

Coult, N., 2006, Explicit formulas for wavelet-homogenized coefficients of elliptic operators: Applied and Computational Harmonic Analysis, **21**, 360–375.

Dablain, M. A., 1986, The application of high-order differencing to the scalar wave equation: GEOPHYSICS, **51**, 54–66.

De Leon, D., 2008, A new wavelet multigrid method: Journal of Computational and Applied Mathematics, **220**, 674–685.

Dorobantu, M., and B. Engquist, 1998, Wavelet-Based Numerical Homogenization: SIAM Journal on Numerical Analysis, **35**, 540–559.

Engquist, B., and O. Runborg, 2009, Wavelet-based numerical homogenization, *in* Highly Oscillatory Problems: Cambridge University Press, London Mathematical Society Lecture Note Series, 98–126.

Engström, C., and D. Sjöberg, 2007, On Two Numerical Methods for Homogenization of Maxwell's Equations: Journal of Electromagnetic Waves and Applications, **21**, 1845–1856.

Fichtner, A., and S. M. Hanasoge, 2017, Discrete wave equation upscaling: Geophysical Journal International, **209**, 353–357.

Gao, K., E. T. Chung, R. L. Gibson, S. Fu, and Y. Efendiev, 2015, A numerical homogenization method for heterogeneous, anisotropic elastic media based on multiscale theory: GEOPHYSICS, **80**, D385–D401.

Grechka, V., and M. Kachanov, 2006, Effective elasticity of fractured rocks: A snapshot of the work in progress: GEOPHYSICS, **71**, W45–W58.

Hanasoge, S., U. Agarwal, K. Tandon, and J. M. V. A. Koelman, 2017, Renormalization group theory outperforms other approaches in statistical comparison be-
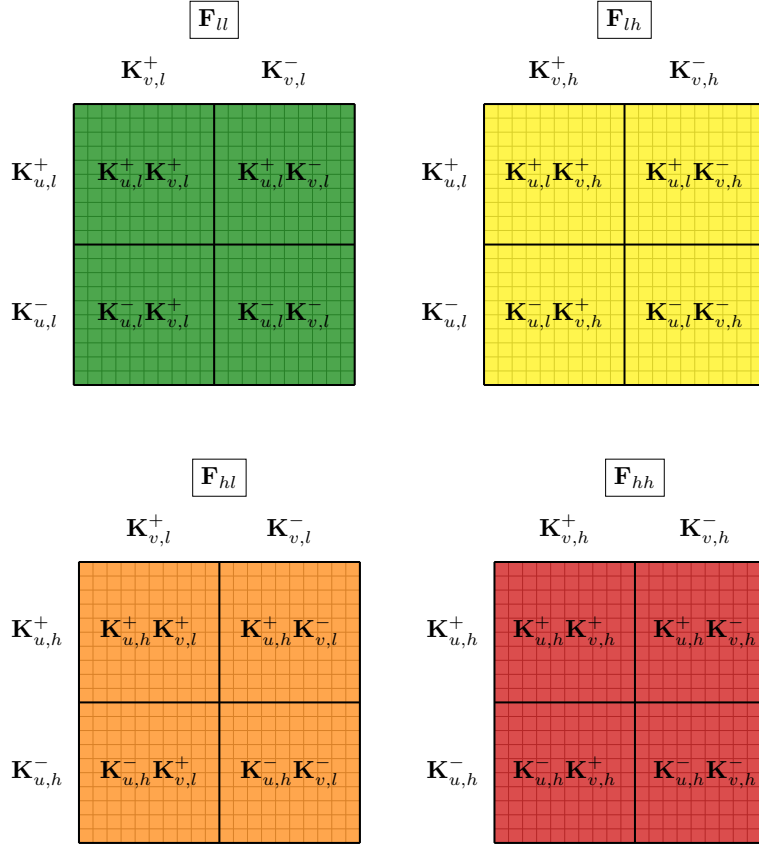
Figure 12: Distribution of wavenumbers for the different parts of modified Fourier operator viz. $\mathbf{F}_{ll}, \mathbf{F}_{lh}, \mathbf{F}_{hl}, \mathbf{F}_{hh}$.

tween upscaling techniques for porous media: Physical Review E, **96**, 033313.

Hanasoge, S. M., 2016, Spatio-spectral concentration of convolutions: Journal of Computational Physics, **313**, 674–686.

Kennett, B. L., and A. Fichtner, 2020, Exploiting seismic waveforms: Correlation, heterogeneity and inversion: Cambridge University Press.

Li, L., J. Tan, D. Zhang, A. Malkoti, I. Abakumov, and Y. Xie, 2021, Fdwave3d: A MATLAB solver for the 3d anisotropic wave equation using the finite-difference method: Computational Geosciences, 1–14.

Malkoti, A., N. Vedanti, and R. K. Tiwari, 2018, An algorithm for fast elastic wave simulation using a vectorized finite difference operator: Computers & Geosciences, **116**, 23–31.

Mishra, N., J. Vondřejc, and J. Zeman, 2016, A comparative study on low-memory iterative solvers for FFT-based homogenization of periodic media: Journal of Computational Physics, **321**, 151–168.

Moulinec, H., and P. Suquet, 1998, A numerical method for computing the overall response of nonlinear composites with complex microstructure: Computer Methods in Applied Mechanics and Engineering, **157**, 69–94.

Persson, P.-O., and O. Runborg, 2001, Simulation of a Waveguide Filter Using Wavelet-Based Numerical Homogenization: Journal of Computational Physics, **166**, 361–382.

Schoenberg, M., and F. Muir, 1989, A calculus for finely layered anisotropic media: GEOPHYSICS, **54**, 581–589.

Song, X., and T. H. Jordan, 2018, Effective-Medium Models of Inner-Core Anisotropy: Journal of Geophysical Research: Solid Earth, **123**, 5793–5813.

Spetzler, J., and R. Snieder, 2004, The fresnel volume and transmitted waves: GEOPHYSICS, **69**, 653–663.

Van Loan, C., 1992, Computational frameworks for the fast fourier transform: SIAM.

Vdovina, T., S. E. Minkoff, and O. Korostyshevskaya, 2005, Operator upscaling for the acoustic wave equation: Multiscale Modeling & Simulation, **4**, 1305–1338.

Wang, Y., 2015, Frequencies of the ricker wavelet: GEOPHYSICS, **80**, A31–A37.

Zijl, W., M. A. N. Hendriks, and C. M. P. 't Hart, 2002, Numerical Homogenization of the Rigidity Tensor in Hooke's Law Using the Node-Based Finite Element Method: Mathematical Geology, **34**, 291–322.